Compressibility Effects on Turbulent Separated Flow in a Streamwise-Periodic Hill Channel — Part 1

Jörg ZIEFLE and Leonhard KLEISER

Institute of Fluid Dynamics, ETH Zürich, Sonneggstrasse 3, 8092 Zürich, Switzerland

Abstract. We present large-eddy simulation (LES) results of the streamwise-periodic hill channel configuration, which is a standard test case for massively separated flows. The Reynolds number (computed with the hill height, the bulk mass flux through the cross-section above the hill crest and the dynamic viscosity at the wall) is chosen as 2800, in accordance with recent DNS data from Peller & Manhart [4] for incompressible flow. The Mach number was varied between Ma = 0.2 and Ma = 2.5. The numerical simulation code NSMB discretises the compressible Navier-Stokes equations with the finite-volume method on a deliberately-chosen coarse structured mesh. The subgrid-scales are accounted for by the well-proven approximate deconvolution model (ADM).
This investigation is an extension of our previous work on this configuration, which focused on the validation of our simulation approach at nearly incompressible flow conditions. In this first part of a two-part contribution [8], the scope lies primarily on the effect of compressibility, especially on the separation characteristics and the flow conditions at the walls. To this end, we introduce a new measure that quantifies reverse flow at the walls and study the distributions of the friction and pressure coefficients. Unlike other investigations of this flow case, we also include the upper wall in this study. Furthermore, we describe the dependence of the turbulence and separation characteristics on the Mach number.

Key words: LES, separation, compressibility, streamwise-periodic hill channel, reverse flow.

1. Introduction

The streamwise-periodic hill channel is a canonical test case for separated flow from curved surfaces. It is based on experiments of Almeida *et al.* [1], with some slight geometric modifications. Figure 1(a) shows a lateral view of the configuration. The bottom and the top of the channel are constrained by solid walls. Periodic boundary conditions are employed in the streamwise (x) and spanwise (y) directions, while at the top and bottom walls no-slip boundary conditions are enforced. All lengths are made dimensionless with the hill height h, henceforth omitted for brevity. The computational domain extends over $L_x = 9$ in the streamwise direction, $L_z = 3.036$ in the vertical direction, and $L_y = 4.5$ in the spanwise direction.
Although the structure of the mean flow field depends on the specific flow conditions, the flow typically separates near the hill top and reattaches somewhere in the flat region between the hills. Due to the highly unsteady character of the separation process, the resulting separation bubble can be recognised only in the mean flow field [9]. An animation of the instantaneous flow fields reveals a periodic but irregular shedding of smaller vortices that are convected downstream. These highly unsteady flow properties lead to long sampling times (about 40-50 flow-through times) in order to obtain sufficiently converged statistics.

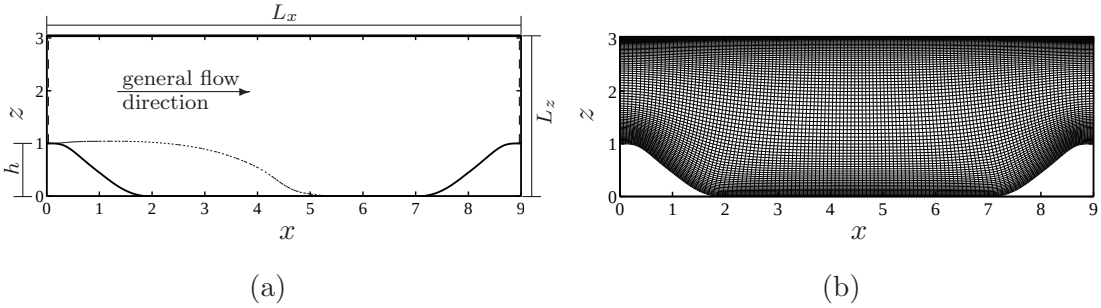

Figure 1. (a) Sketch of the periodic-hill channel and (b) computational mesh used for the LES. The dotted line in (a) denotes the edge of the mean flow recirculation zone with clockwise orientation.

The first incompressible DNS of the configuration at the present Reynolds number of 2800 was conducted recently by Peller & Manhart [4]. An extensive study of the flow physics in the streamwise-periodic hill channel was presented in the LES-based study [2]. This publication, as well as the preceding work that it summarises [5, 6], is based on an approximately four times higher Reynolds number of 10595.
In our previous paper on the periodic-hill channel [9], we compared results of our low-Mach number LES to the above-mentioned incompressible reference data at both Reynolds numbers. The work was aimed at the assessment and validation of our simulation approach using the approximate-deconvolution subgrid-scale model (ADM) for unsteady separated flows. Despite our deliberately-chosen coarse resolution and our compressible simulation method, we found our results to be in good agreement with the comparison data for most quantities. Most notably, the hard-to-predict separation and reattachment locations of the mean flow and the mean velocity profiles were found to be in excellent agreement. In the present work, we extend the previous study to higher Mach numbers up to the supersonic regime. For reasons of computational economy, we restricted our computations to the lower of the two Reynolds numbers (Re = 2800). The focus lies on the physical aspects of the flow, especially the Mach number dependence of the separation characteristics and the flow properties at both walls.
The parameter study was conducted by performing simulations with successively increasing Mach number, thereby using an instantaneous flow field of one simulation as an initial condition for the simulation at the next higher Mach number. Details about the present computational setup, which is the same as in our previous study, can be found in [9]. Table 1 summarises the key parameters and the mean separation and reattachment locations of the present simulations and the reference DNS.

2. Results

In the leftmost picture of figure 2(a), the mean (*i. e.*, spanwise- and time-averaged) streamwise velocity profiles at Ma = 0.2 are compared to incompressible DNS data of Peller & Manhart [4]. Despite of the present coarse resolution, excellent agreement is achieved. In our previous publication [9], this validation was extended, with similar results, to other statistical quantities and important flow features such as separation and reattachment locations. The left column of figure 2 also shows the contours of the mean streamfunction for all five investigated Mach numbers. At Ma = 0.2 this

Table 1. Calculation parameters, mesh dimensions, and separation/reattachment locations of the present and reference simulations. The cross-sectional Reynolds number above the hill crest is Re = 2800 in all cases.

Simulation		Ma	$N_x \times N_y \times N_z$	Mio. Cells	x_{sep}	x_{reatt}
Peller & Manhart (DNS) [4]		n/a	$464 \times 304 \times 338$	47.68 ($\hat{=}$100%)	0.21	5.41
Present LES	(a)	0.2	$128 \times 72 \times 69$	0.64 ($\hat{=}$1.33%)	0.21	5.14
	(b)	0.7			0.28	5.40
	(c)	1.0			0.33	6.06
	(d)	1.5			0.39	5.33
	(e)	2.5			0.46	7.58

is characterised by a large recirculation region downstream of the hill, and a small separation bubble at its windward foot. Additionally, at the leeward hill face a small secondary separation bubble with opposite orientation is contained in the primary recirculation zone. With increasing Mach numbers, the separation bubbles grow and the reattachment point moves farther downstream. They merge for Ma > 1.5, and one large recirculation region covers the lower wall between the hills. Additionally, at the two supersonic Mach numbers the flow also separates at the upper wall due to the presence of an extended region with a large adverse pressure gradient.

The primary reason for the growth and the downstream movement of the recirculation zone with increasing Mach number is the inverse relationship between the Mach number and the heat transfer coefficient, $k \sim 1/\mathrm{Ma}^2$. With rising Mach number, the heat transfer coefficient decreases, thus the increasing amount of heat generated by dissipation in the turbulent flow is less easily transported out of the fluid body through the isothermal walls. As a consequence, the fluid temperature rises. Since the dynamic viscosity is directly dependent on the temperature, $\mu \sim T^{0.7}$, the increased fluid temperature comes along with a higher fluid viscosity. The effect is similar to reducing the Reynolds number of the flow, which is generally known to result in a downstream movement of the separation and reattachment locations [9].

As apparent from visualisations of the instantaneous flow field, there is considerable backflow along the walls at all times. To better quantify this phenomenon, we analysed the time fraction at which the wall-parallel velocity just above the wall $\underline{u} \cdot \underline{t}_{\mathrm{wall}}$ is negative, *i. e.*, $r(x) = \int_{t_0}^{t_0+\Delta T} [1 - H(\underline{u}(x,t) \cdot \underline{t}_{\mathrm{wall}})]\, \mathrm{d}t/\Delta T$ (with the wall-tangent vector in positive x direction $\underline{t}_{\mathrm{wall}}$ and the Heaviside step function H). The result is displayed in the second column of figure 2. At the lower wall, the flow acceleration and the resulting very high velocities above the hill crest prevent backflow, thus the backflow fraction is almost zero. Just downstream of the hill crest, the flow separates and vortices are shed, yielding a sharply rising backflow fraction with a peak of more than 70% backflow. This location lies just downstream of the mean-flow separation point and exhibits the second-largest magnitude of backflow along the bottom wall. Due to the secondary recirculation zone with opposite orientation, which is embedded in the main separation bubble, the fraction of backflow is decreasing rapidly by a considerable amount. The backflow rates grow again at a slower rate downstream of the secondary separation region. For most Mach numbers, a little local maximum appears in the strongly-curved region at the leeside foot of the hill. Downstream of that dent, the fraction of backflow

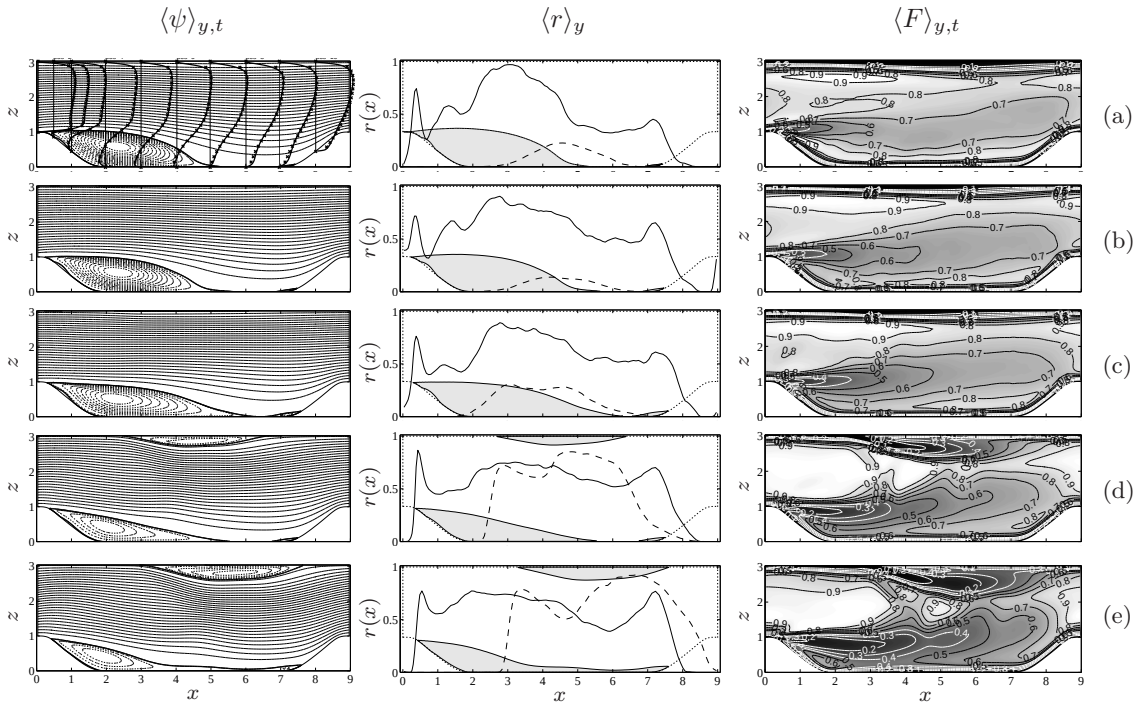

Figure 2. First column: contours of the mean streamfunction $\langle\psi\rangle_{y,t}$ (——positive values, ····· negative values, ——$\langle\psi\rangle_{y,t} \equiv \langle\psi_{\text{wall}}\rangle_{y,t}$) and, in plot (a), mean streamwise velocity profiles, ——present LES results, × incompressible DNS data [4]. Second column: fraction of the spanwise-averaged backflow $\langle r\rangle_y$ at ——lower wall and - - - -upper wall. ——Boundary of mean-flow separation region (shaded in grey), ····· domain boundaries. Third column: contours of the mean Lumley flatness parameter $\langle F\rangle_{y,t}$. (a) Ma = 0.2, (b) Ma = 0.7, (c) Ma = 1.0, (d) Ma = 1.5, (e) Ma = 2.5.

is increasing again to a global maximum, which is located near the streamwise coordinate of the centre of the primary mean-flow separation bubble. Downstream of this maximum, the backflow ratio decreases moderately, until is reaches a plateau around the mean-flow reattachment location. It remains between 40% and 50% in the flow recovery region, until it grows again somewhat due to the small separation bubble at the windward hill foot. Farther downstream, the flow accelerates strongly, and the ratio of backflow sinks fast. Along the second half of the windward hill face ($z > 0.5$), the backflow rate is negligible. An exception occurs for the two Mach numbers Ma = 0.7 and 1.0, where the backflow ratio rises again upstream of the hill crest. Also note the kink of the backflow ratio graph at the end of the curved region of hill foot ($x \approx 8$), which is potentially due to wall curvature effects.

At the upper wall, the backflow rates are negligible for the simulations without the presence of a detached boundary layer, *i. e.*, up to Ma = 1.0. Significant backflow is only occurring in the range $3 \leq x \leq 6$, which coincides with the location of the mean-flow recirculation region for the two highest Mach numbers. Note that the backflow decreases from Ma = 0.2 to 0.7, while it rises considerably by a factor of about two to the next higher Mach number, Ma = 1.0. Additionally the curve changes its shape slightly to a dual-peak form (with maxima at $x \approx 3$ and 5, respectively) that gets more distinct for the higher Mach numbers exhibiting a detached boundary layer. For the two highest Mach numbers Ma = 1.5 and Ma = 2.5, a strong adverse pressure

gradient causes the upper-wall boundary layer to detach, and a large recirculation zone develops. This separation bubble leads to very high backflow rates of 70%-80%, which are of the same magnitude as the values observed in the recirculation region above the lower wall. The large backflow rates are observed primarily in the streamwise range of the mean-flow separation region $3 \leq x \leq 7$. However, while the curve rises sharply from almost zero at the upstream edge of the recirculation region, its decay back to very low values at the downstream end of the separation bubble occurs much more gradually until above the upper half of the windward hill side ($8 \leq x \leq 9$). Within the range of the recirculation region, the graph exhibits the two-peak shape mentioned above. After a local maximum at the upstream edge of the separation bubble, the backflow rates decrease somewhat, until they rise again to a higher, global maximum in the second half of the detached boundary layer. Since increasing Mach numbers lead to stronger pressure gradients, the boundary-layer detachment and thus the upper-wall recirculation region intensifies, resulting in generally higher backflow rates. It is surprising, however, that significant backflow is already occurring in this region at very low Mach numbers such as Ma = 0.2. This leads to the conclusion that already at this Mach number, the adverse pressure gradient exerts a strong effect on the upper-wall boundary layer.

Lumley's flatness parameter F [3], displayed in the third column of figure 2, allows for an analysis of the turbulence characteristics of the flow. While the observed values of F reach levels that are very close to zero, *i. e.*, two-dimensional turbulence, the maxima of F (about 0.9 throughout all Mach numbers) lie considerably below the value for three-dimensional turbulence, $F = 1$. This result is typical for channel flow and can be explained by the nature of the flow configuration and the low Reynolds number. The specific geometry, including the separated boundary-layer downstream of the hill, as well as the influence of the upper and lower walls, does not allow for the development of truly three-dimensional isotropic turbulence. On the other hand, two-dimensional turbulence characteristics are enforced in wall-bounded turbulence by the presence of solid walls. For the three lower Mach numbers Ma = 0.2, 0.7 and 1.0, high values of F are present in the whole upper channel part between the upper-wall boundary layer and the shear layer ($z > 1$), and in the lower channel part ($z < 1$) between the lower-wall boundary layer and the shear layer. The highest flatness values with almost three-dimensional turbulence occur in distinct elongated patches in the high-velocity region above the leeward hill face, close to the upper wall. With increasing Mach number, this area grows in streamwise size and thickens somewhat, but in the major part of the remaining channel, the level of F is considerably lower. This is in contrast to the result for the two highest Mach numbers Ma = 1.5 and 2.5, where the area with the highest values of F (and thus almost three-dimensional turbulence structure) covers almost the complete cross-section between the shear layer and the upper-wall boundary layer, and is only interrupted by its separation and the upward-extending influence of the shear layer in the middle of the channel (at $x \approx 4.5$).

As expected, the values of F are very small in the boundary layers at the lower and upper walls for all Mach numbers. In Figures (a)-(c), the thickening of the upper-wall boundary layer due to the adverse pressure gradient can be well observed. For the two highest Mach numbers Ma = 1.5 and 2.5 the detached upper-wall boundary layer is evident from the considerably thicker region with two-dimensional turbulence for $3 \leq x \leq 7$. Near the lower wall, two-dimensional turbulence is prevalent in the

shear layer downstream of the hill crest, whose characteristics are only gradually displaced by that of the surrounding flow. With increasing Mach number, this region of two-dimensional turbulence extends farther downstream and gains in thickness. At the highest Mach number, the turbulence is primarily two-dimensional in the major part of the domain between the hills ($z < 1$), an exception being the core of the mean-flow recirculation region above the leeward hill foot ($x \approx 1.75$).

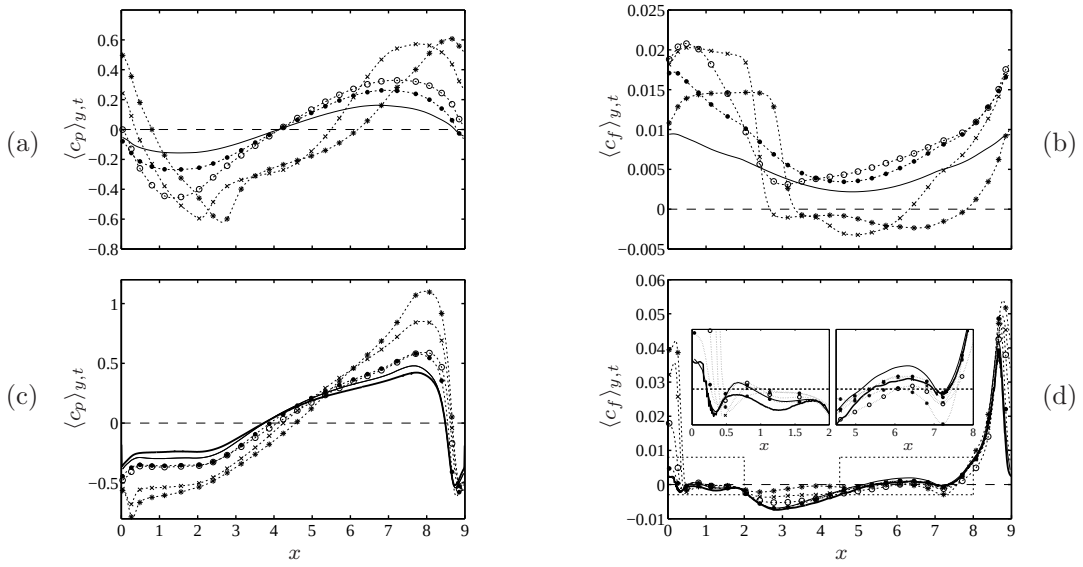

Figure 3. (a)/(c) Mean pressure coefficient $\langle c_p \rangle_{y,t}$ and (b)/(d) mean friction coefficient $\langle c_f \rangle_{y,t}$ at top/bottom wall. —— Ma = 0.2, ···●··· Ma = 0.7, ···○··· Ma = 1.0, ···×··· Ma = 1.5, ···∗··· Ma = 2.5, ——incompressible DNS data [4]. ····· Magnified areas in (d).

In figure 3 we present the streamwise development of the mean pressure and friction coefficients along both walls for the five investigated Mach numbers. Additionally, at the lower wall DNS data from [4] is displayed for comparison. (For the upper wall, no data is available from literature.) Note that the pressure coefficient has been centred by subtracting its streamwise mean value, so that the mean pressure coefficient vanish. This allows for a comparison with the incompressible reference data, where the pressure coefficient is usually presented in this manner due to the lack of a reference pressure.

For the mean pressure coefficient c_p at the lower wall in figure (c), our Ma = 0.2 simulation lies close to the incompressible reference data. The small deviations can be attributed to effects of compressibility in conjunction with the normalisation method [9]. Slightly upstream of the hill crest ($x \approx 8.75$), the pressure reaches a global minimum due to the very high velocities in this narrow cross-section. After crossing the peak of the hill, the flow decelerates and the pressure rises. At $x \approx 0.25$, which roughly marks the beginning of the primary recirculation zone, the pressure stagnates at a low level along the leeward hill face. At the beginning of the flat region between the hills, the pressure rises again. In the first half of the plane region, the increase is somewhat stronger. Around the mean reattachment location, the slope of the curve gets flatter, and the pressure coefficient grows with an almost constant gradient in the recovery region until the stagnation zone around $x \approx 7$ at the windward hill foot. Here the pressure reaches its global maximum and falls quickly along the windward hill face, where the flow is subject to strong acceleration.

Within the high subsonic and transonic regimes, *i. e.*, for Ma = 0.7 and 1.0, the development of the pressure coefficient is very similar to the one at Ma = 0.2. Most notably, the pressure gradient between the hills is larger, leading to more distinct peaks. In the range $0 \leq x \leq 4.5$, the development of the gradient of the pressure coefficient is approximately the same for all three subsonic Mach numbers. (Differences in magnitude of c_p are primarily due to the chosen normalisation.) In the downstream half of the channel ($x \geq 4.5$), the curves for the two higher Mach numbers deviate notably from Ma = 0.2 by rising stronger. Furthermore, the maximum pressure coefficient is reached slightly farther downstream, which coincides with the downstream-movement of the stagnation region for increasing Mach numbers. Between Ma = 0.7 and 1.0 the differences are marginal. A drastic change in form and magnitude of the c_p distribution can be observed in the supersonic regime. Here the mean separation point lies considerably farther downstream. Furthermore, the velocity maximum is not reached slightly upstream of the hill crest but near the mean separation point. Consequently, the pressure minimum also occurs downstream of the hill crest. Slightly farther down the hill, the wall is covered by the relatively slowly moving fluid of the recirculation region, thus the pressure coefficient rises sharply. For Ma = 1.5 a short plateau is recognisable which reaches roughly to the hill foot. At Ma = 2.5, the pressure coefficient begins to rise immediately, albeit at a weaker rate along the windward hill face. Downstream of $x \approx 2$, the pressure coefficient curves for both supersonic Mach numbers rise roughly parallel to each other at a considerably steeper slope than for the three lower Mach numbers. As a result of the strong influence of compressibility, the pressure maxima in the stagnation region above at the windward foot of the hill lie much higher than in the subsonic and transonic regimes. As expected, the pressure coefficient maximum at Ma = 2.5 considerably surpasses the one at Ma = 1.5 and occurs slightly farther downstream.

The pressure coefficient c_p at the flat upper wall of the configuration, depicted in figure 3(a), generally exhibits smaller variations than at the lower wall, which are however in the same order of magnitude. For the three lower Mach numbers its distribution is quite regular. The appearance resembles a sinusoidal shape, with the lower part of the curve occurring in the first channel half ($0 \leq x \leq 4$), and the positive semi-oscillation appearing in the second channel half. The physical explanation of this pattern lies in the effect of the contour of the lower wall on the flow. The strong acceleration caused by the hill contraction causes a pressure drop above the hill (*i. e.*, for $7 \hat{=} -2 \leq x \leq 2$), with a minimum appearing approximately at the location of the maximum velocity, *e. g.*, at $x \approx 1$ for Ma = 0.2. Downstream of the hill the channel cross-section expands and the flow decelerates, resulting in rising pressures. The maximum pressure is reached roughly vertically above the stagnation zone at the foot of the hill. The following contraction of the channel yields increasing velocities and falling pressures. While the curves of all three Mach numbers Ma = 0.2, 0.7 and 1.0 exhibit very similar shape, there are some minor differences. Of course, there are generally larger pressure differences within the flow for the higher Mach numbers due to compressibility. Therefore, their extremal values are higher. Additionally, the locations of the maximum as well as the minimum values of c_p move downstream with rising Mach numbers. This is in agreement with our above findings, where all characteristic locations such as separation and reattachment location move downstream with increasing Mach number. It is however striking that all three curves intersect in the same streamwise location of $x \approx 4.25$, at $c_p \approx 0$ in the chosen

normalisation. Note that the pressure drop takes place over a considerably shorter streamwise length than the following pressure increase. This again correlates with the contour of the lower wall, where the hill causing the flow acceleration extends over a much shorter streamwise stretch than the flat region between the hills, where the flow decelerates.

In the supersonic range, the separation of the boundary layer at the top wall yields a more complex pressure coefficient distribution. Here also the previously observed oscillating pattern appears, but the amplitudes of the minimum and maximum values are even higher and about of the same magnitude for both Ma = 1.5 and 2.5. Additionally, the pressure maxima occur farther downstream and well above the windward hill face, at $x \approx 8$ for Ma = 1.5 and at $x \approx 8.5$ for Ma = 2.5, *i. e.*, shortly above the hill crest. The pressure drop following the maximum extends along the whole leeward hill face and is much steeper in the supersonic range than observed for the three lower Mach numbers. Note that for Ma = 2.5, the slope of the curve exhibits a kink at $x \approx 2$, where the hill face bends into the flat region, and the decrease of c_p continues at a slightly steeper slope. This slight curvature effect can be also observed for other mean quantities. In both supersonic cases, the separation of the boundary layer is preceded by a sharp pressure rise approximately 0.5 hill heights upstream of the separation point, which is located at $x \approx 2.7$ for Ma = 1.5 and at $x \approx 3.25$ for Ma = 2.5. Within the recirculation region, the pressure first continues to rise at a lower rate. Roughly at the thickest part of the separation bubble, the c_p distribution steepens and rises until the maximum above the hill is reached. For Ma = 2.5, the pressure maximum appears quite distinct and exhibits small curvature, whereas for Ma = 1.5 and the lower Mach numbers the curve around the maximum is rounder.

Strong compressibility effects, especially at the hill crest, are evident from the mean friction coefficient c_f at the lower wall in figure 3(d). Again our lowest Mach number case reproduces the DNS data very well. After a sharp peak at $x \approx 8.5$, *i. e.*, still at the windward side of the hill, where very high velocities occur, the friction coefficient drops steeply until the hill crest. Here c_f reaches a short plateau until the mean separation point, where it drops slightly into the negative range. Shortly thereafter it changes its sign again, revealing a confined secondary recirculation region with opposite orientation embedded into the primary separation bubble. Downstream thereof, c_f remains quite constant at negative values close to zero until the foot of the hill at $x \approx 2$. At this point the friction coefficient drops further to its global minimum at $x \approx 2.8$, where it begins to rise slowly, leading to its sign reversal, which marks the mean reattachment point at $x \approx 4.7$. In the post-reattachment zone, c_f exhibits only small positive values, until it experiences a short dip into the negative range at the windward hill foot ($x \approx 7.2$). Here the flow stagnates, and a small recirculation zone appears. The following strong flow acceleration can be witnessed by the steep increase of the friction coefficient along the windward hill face. The c_f distribution does not change considerably over the whole range of Mach numbers. With increasing Mach number, the peak of the friction coefficient rises somewhat and wanders downstream. The short region with constant c_f after the hill crest occurs at a much higher level for the higher Mach numbers. At Ma = 1.5 and 2.5, a second short peak of c_f at slightly lower values than their global maxima is visible, before the friction coefficient drops strongly into the negative range. The secondary separation bubble is also affected by the Mach number. It grows and

moves downstream towards the foot of the hill for higher Mach numbers. In the supersonic range, it appears much flatter but considerably more elongated, and ranges over a large part of the lower hill face until it bends towards the flat region. The dip of c_f to lower negative values in the flat region downstream of the hill foot gets less pronounced with higher Mach numbers. Instead, the reattachment points move farther downstream. For Ma = 2.5, the friction coefficient remains negative throughout the flat region (although it runs very close to zero at $x \approx 6$), and the primary recirculation zone covers the bottom walls between the hills. This results in a more pronounced local minimum of c_f at the stagnation region near the windward hill foot. In the other simulations, there is a small separation bubble which grows from Ma = 0.2 to 1.0 and appears again smaller for Ma = 1.5. However, the negative values of c_f in this region are quite similar for all those simulations.

The magnitude of the friction coefficient c_f at the upper wall, see figure 3(b), lies in the same range as on the lower wall. While for Mach numbers up to Ma = 1.0 the pressure coefficient distribution exhibited only minor differences, the friction coefficient is subject to larger variations along the upper domain boundary. For Ma = 0.2, c_f is highest above the hill crest, where very high velocities occur. The flow decelerates and c_f sinks, as the channel and its "virtual contour" (the cross-section bounded by the upper wall and the boundary of the mean-flow recirculation zone) expand. The minimum friction coefficient, less than half of its maximum, is reached roughly vertically above the mean reattachment location. In the following flow acceleration, c_f rises at approximately the same rate as it decreases before. The friction coefficient at Ma = 0.7 follows the same general distribution as for Ma = 0.2, but at a higher level. While the minimum values are similar, the maximum friction coefficient lies considerably higher at Ma = 0.7. At Ma = 1.0 the peak is located even higher and downstream of the hill crest, at $x \approx 0.5$. The friction coefficient then falls quite steep to a minimum at $x \approx 3$, which lies significantly farther upstream than for the lower Mach numbers, but still at a comparable magnitude. Farther downstream c_f is subject to a quite steady rise which steepens at the windward hill foot. For the two supersonic Mach numbers, the adverse pressure gradient at the upper wall is so large that the boundary layer separates. This results in a major change of appearance in the distribution of the friction coefficient. At Ma = 1.5, its maximum is reached approximately at the same position and magnitude as at Ma = 1.0, slightly downstream of the hill crest. However, the immediate strong drop occurring there is delayed until $x \approx 2$. This coincides with the location where the pressure coefficient reaches its minimum and is approximately 0.5 hill heights upstream of the separation point, where the friction coefficient changes sign. Within the recirculation zone, c_f first remains close to zero and experiences a dip at $x \approx 4$, where the pressure gradient increases. The minimum friction coefficient is located at $x \approx 5$, at less than one fourth of the magnitude of the maximum. Downstream of this location c_f rises at relatively constant slope, except for a kink at $x \approx 7$, which is also visible for the lower Mach numbers. It is an effect of the beginning cross-sectional contraction caused by the contour of the lower wall. The general appearance of the upper-wall friction coefficient at Ma = 2.5 is similar to Ma = 1.5. However, its maximum reaches only 3/4 of the previous value. On the other hand, the plateau of the maximum is wider, so that the drop in c_f preceding the separation region and the recirculation zone itself occur about 0.5 farther downstream. Additionally the extent of the recirculation zone is considerably longer and reaches until $x \approx 7.5$.

3. Conclusions

We extended our previous study of the streamwise-periodic hill channel configuration at nearly incompressible flow conditions to Mach numbers up to Ma = 2.5. The present series of large-eddy simulations was performed on a deliberately-chosen coarse grid using the well-proven approximate deconvolution subgrid-scale model with the finite-volume flow solver NSMB.
In this first paper of a two-part contribution [8], we investigate the Mach-number dependence of the separation characteristics with an analysis of the mean stream-function, and study the flow conditions at the walls in detail using distributions of the mean pressure and friction coefficients. In contrast to previous works, we also consider the flow behaviour at the top wall. We introduce a new quantity, the backflow fraction r, to determine the time fraction of instantaneous backflow along the walls. The turbulence structure is analysed using Lumley's flatness parameter. We are currently extending our research to more complex separated flows by studying two configurations of a jet in crossflow, a generic case [7] and a case related to film-cooling.

Acknowledgements

All simulations were performed at the Swiss National Supercomputing Centre (CSCS). We would like to thank Jan Vos for fruitful discussions and technical support.

References

[1] G. P. Almeida, D. F. G. Durão, and M. V. Heitor. Wake flows behind two-dimensional model hills. *Experim. Therm. Fluid Sci.*, 7:87–101, 1993.

[2] J. Fröhlich, C. P. Mellen, W. Rodi, L. Temmerman, and M. A. Leschziner. Highly resolved large-eddy simulation of separated flow in a channel with streamwise periodic constrictions. *J. Fluid Mech.*, 526:19–66, 2005.

[3] J. L. Lumley. Computational modeling of turbulent flows. In *Advances in applied mechanics*, volume 18, pages 123–176. Academic Press, 1978.

[4] N. Peller and M. Manhart. DNS einer Kanalströmung mit periodisch angeordneten Hügeln. In *STAB (Arbeitsgemeinschaft "Strömung mit Ablösung") Jahresbericht 2004*, pages 178 f., 14. DGLR/STAB Fachsymposium, November 16–18, 2004, Bremen, Germany, 2004.

[5] L. Temmerman and M. A. Leschziner. Large eddy simulation of separated flow in a streamwise periodic channel constriction. In E. Lindborg, A. Johansson, J. Eaton, J. Humphrey, N. Kasagi, M. Leschziner, and M. Sommerfeld, editors, *Turbulence and Shear Flow Phenomena 2*, volume 3, pages 399–404, 2001.

[6] L. Temmerman, M. A. Leschziner, C. P. Mellen, and J. Fröhlich. Investigation of wall-function approximations and subgrid-scale models in large eddy simulation of separated flow in a channel with streamwise periodic constrictions. *Int. J. Heat Fluid Flow*, 24(2):157–180, 2003.

[7] J. Ziefle and L. Kleiser. Large-eddy simulation of a round jet in crossflow. In *36th AIAA Fluid Dynamics Conference*, San Francisco, USA, June 5–8 2006, 2006. AIAA Paper 2006-3370.

[8] J. Ziefle and L. Kleiser. Compressibility effects on turbulent separated flow in a streamwise-periodic hill channel — part 2. In *Notes on Numerical Fluid Mechanics and Multidisciplinary Design*. Second DESider Symposium on Hybrid RANS-LES Methods, Corfu, Greece, June 17/18 2007, Springer, 2007.

[9] J. Ziefle, S. Stolz, and L. Kleiser. Large-eddy simulation of separated flow in a channel with streamwise-periodic constrictions. In *17th AIAA Computational Fluid Dynamics Conference*, Toronto, Canada, June 6–9, 2005. AIAA Paper 2005-5353.